

Article

Ordered Mesoporous TiO₂: The Effect of Structure, Residual Template and Metal Doping on Photocatalytic Activity

Ahmed M. Mohammed ^{1,2}, Ahmet E. Becerikli ³, Simon Ristig ³, Norbert Steinfeldt ¹ and Jennifer Strunk ^{1,*}

¹ Department of Heterogeneous Photocatalysis, Leibniz Institute for Catalysis, Albert-Einstein-Str. 29a, 18059 Rostock, Germany; ahmed.muthafer@uemosul.edu.iq (A.M.M.); norbert.steinfeldt@catalysis.de (N.S.)

² Department of Chemistry, College of Education for Girls, University of Mosul, Mosul 41002, Iraq

³ Max Planck Institute for Chemical Energy Conversion, Stiftstraße 34–36, 45470 Mülheim an der Ruhr, Germany; becer@gmx.de (A.E.B.); simon.ristig@cec.mpg.de (S.R.)

* Correspondence: jennifer.strunk@catalysis.de; Tel.: +49-381-1281-375

Abstract: Using a series of ordered mesoporous TiO₂ (om-TiO₂) with and without Ce or Cu doping, the effects of structure, metal doping and residual template species in the structure are systematically evaluated in terms of products formed during a CO₂ photoreduction process. It is found that the ordered mesoporous structure contributes significantly in the hydrogen evolution reaction from the splitting of gaseous water. No cocatalyst was needed to achieve high hydrogen yields. While carbon-containing products are also observed, the presence of remainders of the organic template used in the synthesis process does not allow an unambiguous identification of the source of products. Small amounts of metal doping do not majorly influence the hydrogen evolution, thus the mesoporous structure can eventually be identified as the main cause for the improved performance.

Keywords: photocatalytic CO₂ reduction; titanium dioxide; mesoporosity; hydrogen production; metal loading



Citation: Mohammed, A.M.; Becerikli, A.E.; Ristig, S.; Steinfeldt, N.; Strunk, J. Ordered Mesoporous TiO₂: The Effect of Structure, Residual Template and Metal Doping on Photocatalytic Activity. *Catalysts* **2023**, *13*, 895. <https://doi.org/10.3390/catal13050895>

Academic Editor: Roberto Fiorenza

Received: 21 March 2023

Revised: 19 April 2023

Accepted: 5 May 2023

Published: 16 May 2023



Copyright: © 2023 by the authors. Licensee MDPI, Basel, Switzerland. This article is an open access article distributed under the terms and conditions of the Creative Commons Attribution (CC BY) license (<https://creativecommons.org/licenses/by/4.0/>).

1. Introduction

Photocatalytic water splitting and the reduction of CO₂ with water into hydrocarbons by semiconductors are considered as promising technologies for a sustainable synthesis of fuels and platform chemicals [1]. A photocatalyst widely applied in the field of energy and fuel generation is titania (TiO₂) [2]. Titania is a low cost, non-toxic, and chemically inert material with a high photostability [3,4]. Three-dimensional titania nanomaterial can be synthesized by sol-gel approach, solvothermal/hydrothermal growth, or by using templates [5].

Recently, mesoporous photocatalysts in general, [6] and titania photocatalysts with mesoporous structures in particular [7,8], have attracted much interest because of their high specific surface area and porous network, leading to an improved diffusion of reactants, better separation of light-generated charge carriers, and increased photocatalytic activity. The synthesis methods of mesoporous titania can be classified in different categories: template free, soft template, hard template, and multi-template routes where each route has its own advantages and disadvantages [8]. For example, the application of soft templates allows the synthesis of mesoporous titania structures with different morphologies and pore sizes ranging from 1-D nanofibers, to 2-D nanosheets, up to 3-D nanostructures. However, the crystallinity of the formed titania structures is relatively low [8]. Zhang et al. synthesized mesoporous TiO₂ comprised of small anatase nanoparticles [9]. The materials that had undergone hydrolysis prior to calcination performed better in photocatalytic CO₂ reduction than the solely calcined materials and as the benchmark P25. The hydrolysis prevents excessive particle growth, retaining a high surface area.

A subclass of mesoporous titania is ordered mesoporous titania (om-TiO₂), in which an array of channels is formed rather than random mesoporosity, which has been proposed

as beneficial for mass transfer [10] and metal dispersion. [11] Om-TiO₂ has been successfully applied in solar cells, lithium-ion batteries, and sensors, and as catalyst support, and photocatalyst [7]. It can be synthesized by sol-gel route using ionic or non-ionic surfactants as a template [12,13] and the size of the ordered mesopores is strongly affected by the used template [7]. In this soft templating pathway, the titanium precursor and the surfactant were co-assembled inside the synthesis mixture. Zimny et al. [14,15] combined the evaporation induced self-assembly (EISA) method with the liquid crystal templating (LCT) pathway. Their synthesized material showed after titania precipitation a hexagonal ordered structure with uniform pore size. A further calcination step led to the formation of semicrystalline walls and the ordered structure was still intact up to a temperature of 450 °C. Moreover, the calcined material showed good photocatalytic activity in the degradation of methyl orange [15]. In contrast to silica-based structures such as SBA-15 the degree of mesoporous ordering of the titania framework decreased with increasing calcination temperature due to the formation of small nanocrystals and their sintering inside the relatively thin framework walls [16]. Liu et al. [17] synthesized om-TiO₂ by the EISA technique using cetyltrimethylammoniumbromide (CTAB) as a liquid crystal template showing a 2D hexagonal mesostructure with small particle size and high specific surface area.

Om-TiO₂ with mixed anatase-rutile crystal structure has been found to be a beneficial hydrogen evolution photocatalyst, even under visible light irradiation [18]. The higher efficiency compared with P25 at comparable phase ratio has mainly been attributed to the higher surface area and the better interfacial contact of the two phases [18]. Jinhua Ye et al. synthesized om-TiO₂ using EISA method [19]. CH₄ was the observed main product in photocatalytic CO₂ reduction, with an improved efficiency of a factor of 71 compared to the reference P25, and still a factor of 53 times compared to non-ordered mesoporous TiO₂. In a comparison of various ordered mesoporous semiconductors prepared by a hard templating method, om-TiO₂ showed considerably improved CH₄ and CO yields compared to the commercial P25 counterpart, but mesoporous ZnS outperformed this material in terms of CH₄ formation [20]. Doping of om-TiO₂ with Co was beneficial to improve the formation of CO and CH₄, with an optimal Co/Ti ratio of 0.025 [21]. Interestingly, an addition of Co beyond this amount lead to the formation of separate cobalt oxide domains and the almost complete suppression of CO formation [21]. A modification of an om-TiO₂ material with gold nanoparticles allowed even the formation of CO and CH₄ under visible light [22].

In this work, the photocatalysts have been synthesized employing coprecipitation using EISA combined with the LCT pathway [16] based on the method developed by Zimny [15]. The effect of a doping with Cu or Ce was tested. Hydrogen evolution was significantly enhanced in the mesoporous structure, but in spite of various attempts to remove the organic template, the formation of carbon-based products could not uniquely be attributed to proper photocatalytic CO₂ reduction. Our results of significant product formation from carbon sources other than CO₂ are particularly relevant for approaches in which organic linkers or CO₂ adsorbers are added to mesoporous TiO₂, [23] highlighting the need for proper blank experiments in such cases. The influence of the dopant was only moderate.

2. Results

2.1. Structural Characteristics of the TiO₂ Samples

The small angle X-ray scattering (SAXS) patterns of the mesoporous materials (Figure 1A) show a d₁₀₀ Bragg reflection which indicates the presence of ordered domains inside the titania framework. The presence of the doping metals (Cu or Ce) had a relatively low impact on the shape of its reflection indicating that low doping levels affect the formation of the ordered mesoporous structure only to a minor degree. The X-ray diffraction (XRD) powder patterns of pristine calcined titania and materials synthesized with 0.5 mol% metal doping are displayed in Figure 1B. All patterns exhibited intense reflections of the anatase phase (International Center of Diffraction Data (ICDD) 03-065-5714) together with low

intense reflections of β -TiO₂ (ICDD 00-035-0088). Bragg reflections from phases containing the doping metal or an expansion of anatase cell volume due to presence of the doping metal were not observed. The average crystallite sizes which were estimated using the Scherrer equation are listed in Table 1. The crystallite size of the pristine om-TiO₂ and of the materials synthesized with 0.5 mol% doping metal were similar and ranged between 4–5 nm.

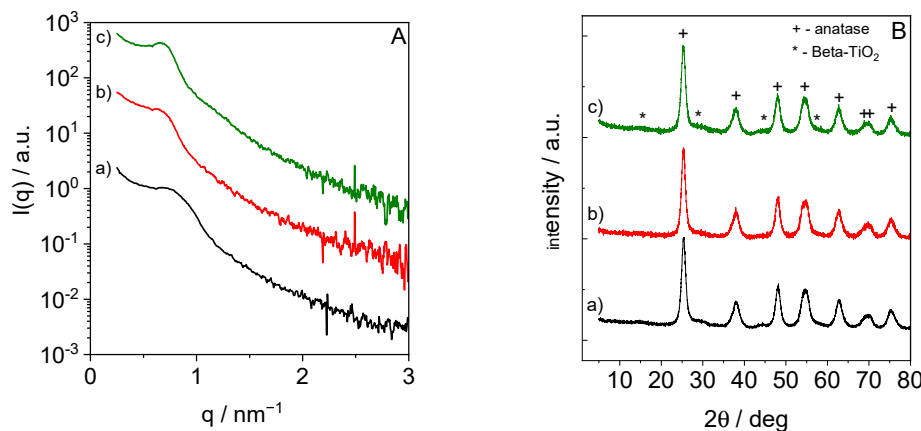


Figure 1. (A) SAXS and (B) XRD powder patterns of pristine and doped TiO₂ materials prepared with 0.5 mol% doping metal after annealing at 450 °C; a—pristine om-TiO₂, b—om-0.5 mol% Cu/TiO₂, c—om-0.5 mol% Ce/TiO₂ (the single SAXS pattern was shifted by multiplication with a constant factor).

Table 1. Characteristics of calcined om-TiO₂ prepared with 0.5 mol% of Cu or Ce; n.d. = not determined.

Sample	Crystal Phase	s m ² /g	V _p cm ³ /g	d _p nm	Cryst. Size * nm	Band Gap eV
P25	Anatase/Rutile	50	n.d.	n.d.	n.d.	3.2
om-TiO ₂	Anatase/ β -TiO ₂	166	0.27	3.9	5	3.17 ± 0.04
0.5 mol% Cu	Anatase/ β -TiO ₂	169	0.23	3.9	5	3.18 ± 0.04
0.5 mol% Ce	Anatase/ β -TiO ₂	135	0.24	3.9	4	3.22 ± 0.04

* Anatase.

2.2. Textural Properties

N₂ adsorption–desorption was applied to explore the pore structure, the Brunauer–Emmett–Teller (BET) surface area, and pore size distribution of the prepared om-materials. The corresponding isotherms of the calcined pristine and doping metal containing titania samples are presented in Figure 2. All samples exhibited a type IV isotherm, which is characteristic for mesoporous materials with hysteresis loops between H2 and H3 [24].

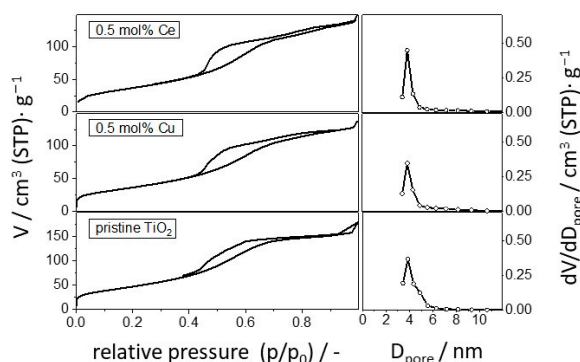


Figure 2. N₂ adsorption–desorption isotherms and pore size distribution of pristine and doped mesoporous om-TiO₂.

The BET surface areas (s), pore volumes (V_p), and maximum of the pore diameter distribution (d_p) are summarized in Table 1. The BET surface area of pristine om-titania and materials synthesized with 0.5 mol% metal doping were relatively high compared to P25. Repeated synthesis (six times) of pristine titania shows an average BET surface area of $176 \pm 16 \text{ m}^2 \cdot \text{g}^{-1}$. The differences in BET surface area between different batches might be attributed to the solvent evaporation step because the geometrical structure of the titania network before precipitation with gaseous ammonia seems to strongly depend on the amount of evaporated solvent. With increasing solvent evaporation time the viscosity of the formed gel increases. Since the viscosity change can only be observed visually, it is difficult to always achieve the same point even if the same time and temperature are used.

2.3. Optical Properties and Surface Composition

The UV/Vis diffuse reflectance spectra (DRS) of the om-materials are presented in Figure 3. DRS spectra of P25, pure CeO_2 , or CuO phase are presented in Figure S1 (Supplementary Materials). The om- TiO_2 sample showed only absorbance in the wavelength region $<400 \text{ nm}$ [25,26] similar to P25 due to band gap excitation, which can be understood as the ligand-metal charge transfer between titanium Ti^{4+} (3 d) and oxygen ligand O^{2-} (2p) [27]. The samples synthesized with 0.5 mol% of doping metal showed some absorption at wavelengths higher than 400 nm. The extent of the red shift was stronger for Cu than for Ce.

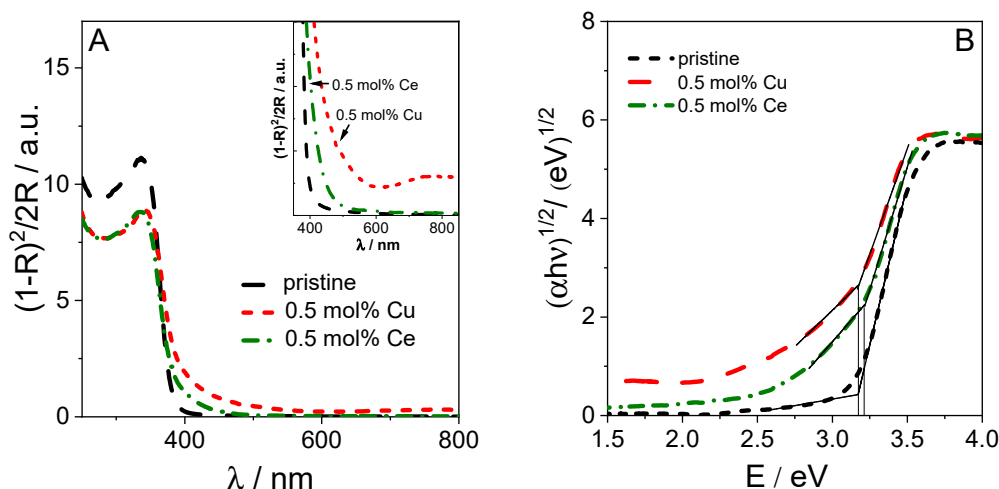


Figure 3. UV/Vis diffuse reflectance spectra (DRS) of (A)—pristine om- TiO_2 and materials synthesized with 0.5 mol% doping metal and (B) the corresponding Tauc plots for estimation of the band gap.

Figure 3b shows modified Tauc plots used for estimation of the band gap [28–30]. The band gap of all three samples was around 3.2 eV (see Table 1) indicating that the low dopant concentration does not affect the TiO_2 band gap energy but it might create additional levels adjacent to the absorption edge.

When Cu was added, absorption shifting occurred at just above 400 nm together with a second absorption band at higher wavelengths. The absorption between 400 and 500 nm was previously attributed to interfacial charge transfer from the O 2p valence band to the Cu^{2+} state attached to TiO_2 [31] or more generally to the formation of a heterojunction between Cu_xO and TiO_2 [32]. The Cu^{2+} state might be present either as $\text{Cu}(\text{II})$ ion, $\text{Cu}(\text{II})$ nanoclusters, or in the form of an amorphous CuO oxide phase [31]. Absorption at wavelengths higher than 550 nm (second band) is mainly due to the d-d transition of Cu^{2+} in the crystalline environment of TiO_2 [31,33], to an interband transition in $\text{Cu}(\text{II})$ clusters deposited over TiO_2 [32], or to the presence of crystalline bulk CuO [34]. The EPR spectrum of the Cu-doped samples is shown in Figure S2. The spectra showed a hyperfine structure of Cu^{2+} ions due to interaction of the electron spin ($S = 1/2$) with its

nucleus spin ($I = 3/2$). The value for the parallel component of the g-tensor was $g_{||} = 2.347$ and the hyperfine splitting amounted to $A_{||} = 110$ G. The values for the normal components could not be resolved. The spectrum indicates the location of Cu^{2+} ions in an axially distorted octahedral environment [31] occupying sites vacated by lattice Ti^{4+} ions [35]. The signal of isolated Cu^{2+} ions seems to be superimposed by a broader peak which results from Cu^{2+} interaction in a CuO cluster. The appearance of a broad Cu^{2+} signal was recently explained by Cu segregation to the titania surface during the crystallization process [36].

TiO_2 samples synthesized with Ce also showed a red shift in the absorption toward longer wavelengths. Absorption until 500 nm was previously observed for CeO_2 phase [37] and connected with the presence of Ce^{3+} ions in mesoporous CeO_2 or $\text{TiO}_2/\text{CeO}_2$ samples [38]. Therefore, it might be assumed that some parts of the Ce^{4+} ions have formed metal oxide clusters, probably located on the surface of titania. Otherwise, a red shift in light absorption was also explained by incorporation of Ce^{4+} ions into the titania lattice where they substitute Ti^{4+} ions [39]. The amount of Ce integrated into the TiO_2 crystallites is expected to be rather low because of the big difference in the ionic radii between Ce^{4+} and Ti^{4+} . This assumption is supported by XRD results (Figure 1B) which show no lattice distortion in the presence of Ce. Figure S3 shows HAADF-STEM images of Ce-doped mesoporous titania. The images confirm the mesoporous structure und support the assumption that Ce is finely distributed inside or on the surface of the titania framework.

The Ti 2p core level XP spectra of the mesoporous titania samples are presented in Figure S4. The Ti 2p binding energy was in the range of 458.4–458.8 which indicates that the titanium ions are mostly present as Ti(IV), whether the TiO_2 was doped or not. Core level O 1 s and C 1 s spectra are shown in Figure 4. The O 1 s spectrum of om- TiO_2 shows a signal at 529.4 eV which is attributed to the lattice oxygen in TiO_2 . The slight shift to higher binding energy in the case of the doped samples might occur from the additional O-Cu or O-Ce bonds. A shoulder peak around 531.7 eV was assigned previously to the presence of physisorbed water. The C 1 s XP spectrum for the three samples is nearly identical, showing the presence of carbon containing C-C, C=O, and C=OOH bonds which originate mainly from the surfactant.

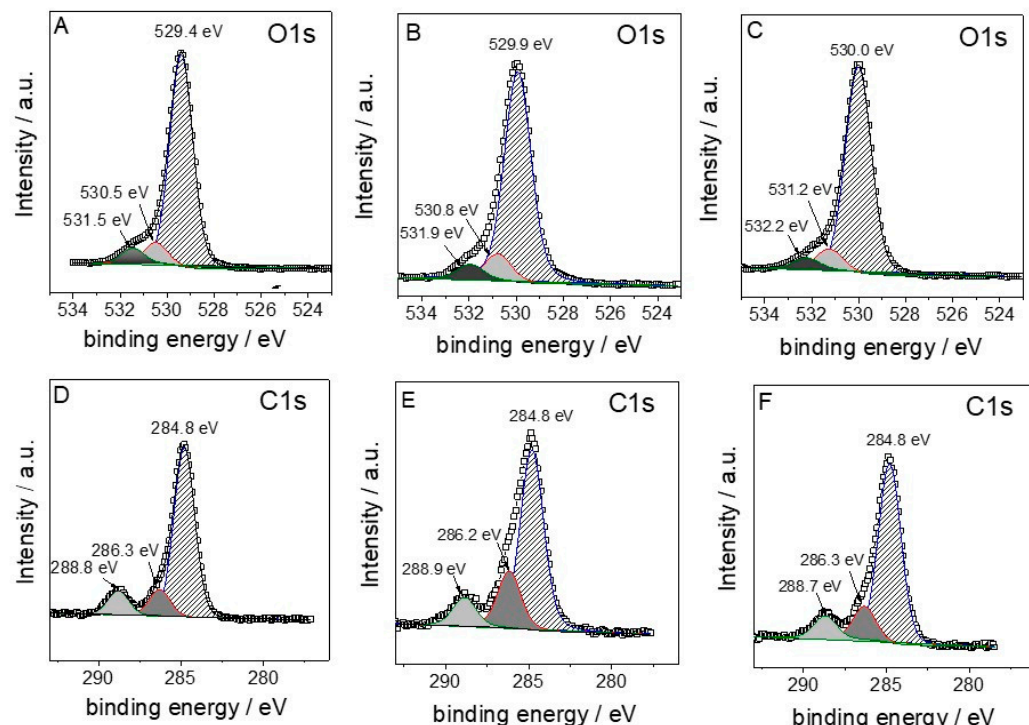


Figure 4. Deconvoluted O 1 s (A–C) and C 1 s (D–F) core level spectra of om- TiO_2 (A,D), om-0.5 mol%Cu/ TiO_2 (B,E), and om-0.5 mol%Ce/ TiO_2 (C,F).

X-ray photoelectron spectroscopy (XPS) was also used to evaluate the surface composition of the materials. In addition to the elements listed in Table 2, the materials also contained small amounts of Si and F, which may result from sealing grease of the used glassware. The low nitrogen content likely originated from the precipitation of the TiO_2 with gaseous NH_3 . The presence of nitrogen indicated that the adsorbed ammonia species were not completely removed from the titania surface during the following surfactant extraction and the thermal annealing. The relatively high surface carbon content indicates that despite repeating the surfactant removal step four times in boiling ethanol, a larger portion of the surfactant was still present on the catalyst surface. The results demonstrate that even after a thermal treatment at $450\text{ }^\circ\text{C}$ in pure oxygen the organic template cannot be removed completely. As will become evident in the following paragraphs, this high carbon loading can act as a carbon pool, leading to formation of carbonaceous species that do not originate from the reaction of CO_2 with the tested photocatalysts.

Table 2. Near surface composition of the different materials determined by XPS.

Sample	Ti Atom%	O Atom%	C Atom%	N Atom%	Dopant Atom%
P25					
pristine om- TiO_2	23.8	55.1	18.8	0.5	n.a.
om- TiO_2 /0.5 mol% Cu	23.8	56.0	18.5	0.6	0.3
om- TiO_2 /0.5 mol% Ce	25.3	52.0	20.1	0.6	0.2

2.4. Effect of Mesoporous Structure and Metal Loading in Product Evolution

The materials were tested in CO_2 photoreduction in the high purity photoreactor presented in detail below. The measurements were conducted in such a way that a CO_2 -free experiment under continuous flow (6000 ppm H_2O in 6 mL min^{-1} He for 45 min, followed by a He flow of 6 mL min^{-1}) preceded a batch experiment, in which CO_2 was also offered to the photocatalyst, to determine simultaneously the reactivity of the samples in CO_2 photoreduction and H_2 evolution. The preceding flow experiment was employed as a method to photocatalytically clean the material from the residual organic template that had been used for the synthesis of the mesoporous structure and from impurities adsorbed on the material from the atmosphere. This process has been described and applied previously [40]. The main product formed in the batch experiments from all mesoporous and metal-modified samples in the presence of CO_2 and light was hydrogen (H_2). The H_2 yields for all samples are presented in Figure 5.

It is evident that the mesoporous structure significantly affects the production of H_2 when compared to P25 which was used as the benchmark material. This fully agrees with an earlier work of ours, [41] in which the low activity of bare P25 for H_2 evolution has been described. The ordered mesoporous TiO_2 (om- TiO_2) sample produces more than an order of magnitude more H_2 than P25- TiO_2 in half the reaction time, with a final yield of $2520\text{ ppm g}_{\text{cat}}^{-1}\text{ h}^{-1}$ (Figure 4). It must be clearly noted that no cocatalyst (such as Pt) was used in this work. Although the surface area increases only ~threefold in the om- TiO_2 material compared to P25, the hydrogen evolution increases by a factor of ~25. Thus, the improvement must be attributed to more than just the larger surface area. Our current study does not allow us to unambiguously trace a specific property of the om- TiO_2 as the cause for the improved performance. The possibilities may be the presence of an increased amount of defect sites in the ordered mesoporous structure, an improved separation and migration of charge carriers, and/or a better diffusion of reactants in the structure, in agreement with Refs. [7,8]. Lastly, also the interface formation between anatase and $\beta\text{-TiO}_2$ in om- TiO_2 , instead of anatase and rutile as in P25, may have a beneficial effect. Further studies are needed to elucidate the specific causes.

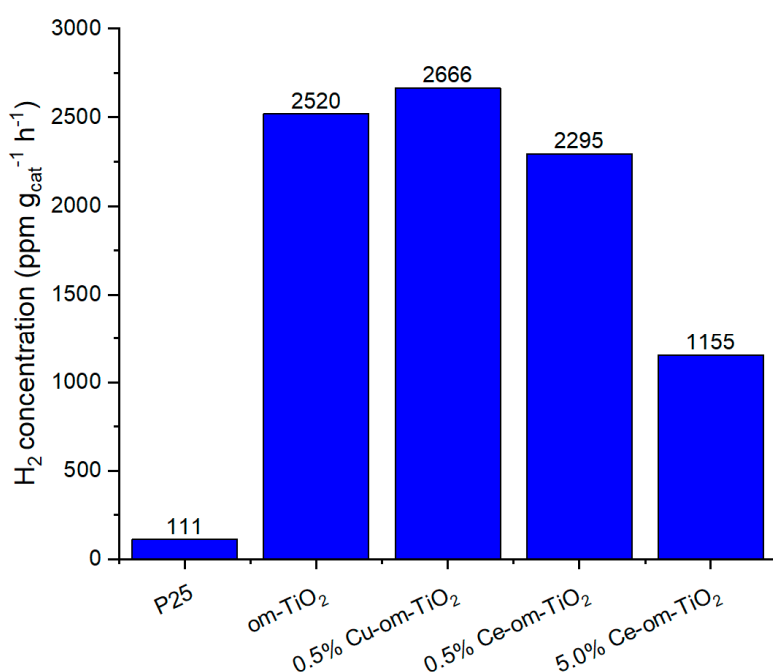


Figure 5. H₂ production from tested samples under batch conditions in the presence of humidified CO₂.

The addition of 0.5%mol of Cu in the mesoporous structure leads to a 5.8% percent increase in H₂ production, from 2520 ppm g_{cat}⁻¹ h⁻¹. The addition of Ce though seems to be detrimental to H₂ production as the 0.5%mol Ce/om-TiO₂ sample exhibited 8.9% less H₂ than the om-TiO₂ sample (2295 ppm g_{cat}⁻¹ h⁻¹). The higher SSA and actual metal loading of the Cu-modified sample could explain the better performance of the om-0.5% mol Cu/TiO₂ when compared to the 0.5%mol Ce one. Similarly, the slightly lower surface area caused by Ce may have an influence, which is in line with our assumption that any direct influence of the dopant on the reaction is small. Another possibility is that Cu causes a slightly improved absorption of visible light (Figure 3). Cu is also more likely to be reduced to a metallic state under irradiation, which may then provide active sites for H₂ formation. As is evident from Figure 5, the presence of the mesoporous structure is the main reason for the much higher H₂ evolution compared to P25. While the addition of Cu leads to an increase in H₂ production the extra cost associated with the preparation of the Cu-doped om-TiO₂ material is not justified by that marginal increase in productivity.

Apart from H₂, C-containing products were also identified when reacting the samples with CO₂. In the case of P25-TiO₂, 66.7 ppm of CO and 17.9 ppm of CH₄ were formed after 4.5 h (Figure S1). In previous studies of ours [40,41] we have reproducibly seen that the main product of CO₂ photoreduction using P25 is CH₄, with a concentration of 80 ppm when using 1.5% CO₂ (in He) and 0.6% H₂O. In the experiments of the current work, a more diluted concentration was selected (0.5% CO₂, 0.6% H₂O), and a much-decreased CH₄ concentration was observed. The product distribution may also be influenced by residual impurities (see below).

For the mesoporous materials, CH₄ and CO and traces of ethane (C₂H₆) were observed (Figure S5). While these identified C-containing molecules might be considered as products of the reaction of CO₂ with the respective samples, this seems not to be the case in these series of measurements (for P25 as well as the mesoporous samples). As was evident from the XPS surface composition analysis of the tested photocatalysts (Table 2), all the mesoporous samples have a carbon-rich surface due to the presence of leftover species from the incomplete removal of the template. These species form a carbon pool which (because of the high thermodynamic stability of CO₂) are likely to react faster than CO₂ under light irradiation. In this way, an overestimation of the efficiency of the samples

toward C-products from CO₂ photoreduction is to be expected. It is clear, though, that even if all C-containing species were considered as products of CO₂ reduction (which they should not), the observed concentration of H₂ formed would be many times higher. For the sake of completeness, the concentrations of the C-containing species formed from the decomposition of the template can be seen in Figure S5. The two metal loaded samples seem to be somewhat more affected by the residual template: much higher amounts of CH₄ were formed in the batch experiments compared to the om-TiO₂ sample (Figure S5). This may indicate that the metal dopant catalyzes the degradation of the residual template. Although the amounts of CH₄ and CO are rather similar regardless of the dopant, C₂H₆ was also observed for the Ce-doped sample (Figure S5).

It may be assumed that the reaction of the leftover species could also be considered the origin of the H₂ formed. However, in an experiment conducted by our group, 100 μL of isopropanol (iPrOH) were added to the surface of a P25 pellet (total mass 1 g) [42]. Then 1.5% CO₂ (in He) was added to the reaction mix and an Hg/Xe lamp (200 W, light intensity 200 mW cm⁻²) was used to irradiate the reaction chamber. While various C-containing molecules were formed, including CH₄, C₂H₆, and C₂H₄, no H₂ product could be identified, i.e., the concentration was below ~20 ppm. Based on these results, the formation of major amounts of H₂ from hydrocarbons leftover in om-TiO₂, especially in the amounts presented in Figure 4, is not likely to occur.

3. Materials and Methods

Triblock copolymer P123 (EO20PO70EO20, Sigma-Aldrich, Darmstadt, Germany) was used as a structure-directing agent (surfactant) and titanium isopropoxide (Ti(OiPr)₄, 97%, Sigma-Aldrich, Germany) was used as the titania precursor. Cerium chloride heptahydrate (CeCl₃·7H₂O, 99.9%) was also purchased from Sigma-Aldrich (Germany). Copper chloride dihydrate (CuCl₂·2H₂O, 99%) and HCl (37%) were obtained from VWR International (Darmstadt, Germany). Absolute ethanol was obtained from J. T. Baker (Darmstadt, Germany). All chemicals were used as received without any further purification.

3.1. Synthesis of Un-Doped and Metal Doped Ordered Mesoporous Titania

An amount of 1 g of P123 was dissolved in 20 g of ethanol in a two-necked round bottom flask (100 mL) at room temperature (RT) under stirring. After 30 min of stirring at RT, 2.1 g of HCl (37%), 3 g of Ti(OiPr)₄, × g of metal source (for more details see Table S1), and 2 g of distilled water were added to the P123-containing solution. Immediately after water addition, the flask was flushed with argon to avoid the formation of a titania precipitate. The two-necked round bottom flask containing the clear reaction mixture was immersed in a water bath which was heated to a temperature of 40 °C. After the reaction mixture had achieved the desired temperature, the argon flow was stopped and the solvent removal was started under reduced pressure (250 mbar). With an increasing amount of evaporated solvent, the pressure was reduced finally to a value of 55 mbar. The gels obtained after solvent evaporation were dried in an oven at 40 °C in air atmosphere for 15 to 18 h. The aged materials were deposited as a thin layer on Petri dishes by using a spatula and placed in a desiccator. The air in the desiccator was exchanged for ammonia and the solid material was treated at RT with ammonia for 18–22 h to allow the TiO₂ precipitation. The P123 surfactant was removed from the titania framework by treatment of the solid material with boiling ethanol for 1 h. This procedure was repeated 4 times. Finally, the obtained powder was heated under argon flow (100 mL/min) from 22–450 °C for 6.5 h and then 2 h under oxygen flow (100 mL/min) at 450 °C. Pristine mesoporous TiO₂ was also prepared using the same procedure without the addition of metal source.

3.2. Characterization

SAXS measurements were carried out using a Kratky-type instrument (SAXSess, Anton Paar, Graz, Austria) operated at 40 kV and 50 mA in slit collimation using a two-dimensional CCD detector cooled to –40 °C or image plates digitalized with a Cyclone

Plus (Perkin Elmer, Downers Grove, IL, USA). A Göbel mirror was used to convert a divergent polychromatic X-ray beam into a collimated line-shaped beam of CuK α radiation ($\lambda = 0.154$ nm). Slit collimation of the primary beam was aimed to increase the flux and to improve the signal quality. The sample cell consisted of a metal body with two windows for the beam. The samples were sealed between two layers of adhesive tape. Scattering profiles of the mesoporous materials were obtained by subtraction of the detector current background and the scattering pattern of adhesive tape from the experimental scattering patterns. The 2D scattering patterns were converted with SAXS Quant software (Anton Paar) into one-dimensional scattering curves as a function of the magnitude of the scattering vector $q = (4/\lambda) \sin(\theta/2)$. Correction of the instrumental broadening effects (smearing) was carried out with SAXS Quant software using the slit length profile determined in a separate experiment. All SAXS measurements were carried out at 25 °C.

XRD powder patterns were recorded either on a Panalytical X'Pert diffractometer (Almelo, the Netherlands) equipped with an Xcelerator detector or on a Panalytical Empyrean diffractometer equipped with a PIXcel3D detector system, both used with automatic divergence slits and Cu K α radiation (40 kV, 40 mA; $\lambda = 0.015406$ nm). The measurements were performed in 0.0167° steps and 25 s of data collecting time per step. Phase analysis was performed with the Panalytical HighScore Plus software package using the PDF-2 2015 database of the ICDD. Crystallite sizes were calculated by applying the Scherrer equation and the usage of the integral breadth under the assumption of spherically shaped crystallites. K is set to 1.0747. The average value of the calculated sizes of diffraction peaks between $20 \leq 2\theta \leq 50$ ° is presented here.

Nitrogen adsorption–desorption isotherms were collected at –196 °C on BELSORP-mini II (BEL Japan, Inc., Osaka, Japan). The specific surface area and pore size distribution were calculated from the adsorption and desorption branches of the isotherm, respectively, applying the BET equation for the N₂ relative pressure range of $0.05 < P/P_0 < 0.3$ and the Barrett–Joyner–Halenda (BJH) method for the pressure range of $0.3 < P/P_0 < 0.99$.

UV/Vis spectra were measured with the AvaSpec-2048 fiber optic spectrometer (Avantes B.V., Apeldoorn, the Netherlands) using the FCR7UV-400-400-2-Me-HT Fiber optic and pure barium sulfate BaSO₄ powder as the white reflection standard of referencing.

The oxidation states and the surface compositions were determined by XPS. The measurements were performed with an ESCALAB 220iXL (Thermo Fischer Scientific, Waltham, MA, USA) with monochromatic Al K α radiation ($E = 1486.6$ eV). The samples were fixed on a stainless steel sample holder with double adhesive carbon tape. For charge compensation a flood gun was used. The spectra were referenced to the C1s peak at 284.8 eV. After background subtraction the peaks were fitted with Gaussian-Lorentzian curves to determine the positions and areas of the peaks. The surface composition was calculated from the peak areas divided by the element-specific Scofield factor and the transmission function of the spectrometer.

3.3. Photocatalytic Experiments

Photocatalytic experiments were conducted in a high purity gas-phase photoreactor system as reported previously [40,41]. The system is designed specifically to prevent carbonaceous impurities resulting from reactor construction. A 200 W Hg/Xe lamp with water filter to remove the IR radiation (UV+vis irradiation with an intensity of approximately 200 mW cm^{−1}) was used for all experiments. The measurement procedure comprised a pure gas-phase water splitting experiment under conditions of continuous flow. High purity helium (purity 99.9999%) at a flow rate of 6 mL min^{−1} was mixed with 0.6% of water using a stainless steel saturator cooled to 5 °C. Water dosing was switched off after 45 min, and from that time onwards, only adsorbed water on the samples was present. Apart from checking the activity in pure water splitting, this measurement also serves to photocatalytically degrade organic impurities still left on the mesoporous titania surface. Gas analysis was carried out with a calibrated online gas chromatograph (Shimadzu TRACERA, Duisburg, Germany) with a barrier discharge ionization detector (BID). The gas analytics

can detect CH₄, CO, CO₂, H₂O, H₂, C₂H₄, C₂H₆, O₂, and N₂. For CH₄, the detection limit is ~0.1 ppm; for all other gases ~1 ppm.

The flow experiment was followed by a batch experiment in which the reactor was filled with 0.5% CO₂ (purity 99.9995%) in helium (purity 99.9999%) to an initial pressure of 1500 mbar. Gas analysis was similar to the system described above. Due to gas sampling from the batch reactor, the pressure in the reactor drops upon each measurement. This pressure drop was corrected for by the calibration curves used for the GC analytics.

4. Conclusions

An ordered mesoporous TiO₂ was presented with very high activity in photocatalytic hydrogen evolution in absence of any cocatalyst. The yields were more than an order of magnitude larger than for commercial P25 and were not just related to the larger specific surface area, which increased only ~threefold. The ordered mesoporous structure, rather than the doping with Cu or Ce, was the main factor leading to the high activity. The dopants had only a moderate effect, which was positive for Cu and detrimental for Ce. Although carbon-containing products were also observed, the inability to completely remove the template from the ordered mesoporous structure makes it impossible to unambiguously assign these species to products from CO₂ reduction. This again highlights the need for proper reference experiments, whenever the synthesis procedure involves considerable amounts of organic species.

Supplementary Materials: The following are available online at <https://www.mdpi.com/article/10.3390/catal13050895/s1>, Figure S1: UV/Vis DRS spectra of pure P25, CeO₂, and CuO. Figure S2: Room temperature EPR spectrum of 0.5 mol% Cu/TiO₂. Figure S3: HAADF-STEM images of om-0.5 mol% Ce/TiO₂ using two different magnifications. Figure S4: Ti 2p XP spectra of (A) om-TiO₂, (B) 0.5 mol% Cu/TiO₂, and (C) 0.5 mol% Cu/TiO₂. Figure S5: Overview of formed carbon-containing species on various samples.

Author Contributions: Conceptualization, N.S. and J.S.; formal analysis, A.M.M. and A.E.B.; investigation, A.M.M., A.E.B. and N.S.; resources, N.S. and J.S.; supervision, N.S. and J.S.; validation, A.M.M., A.E.B., S.R. and N.S.; visualization, A.M.M. and N.S.; writing—original draft, A.M.M., N.S. and J.S.; writing—review and editing, S.R., N.S. and J.S. All authors have read and agreed to the published version of the manuscript.

Funding: This research received no external funding. The APC was funded by the Leibniz Institute for Catalysis.

Data Availability Statement: Data is available from the authors upon reasonable request.

Acknowledgments: We would like to thank Stephan Bartling and Henrik Lund, Leibniz Institute for Catalysis, for the XPS and Powder XRD measurements, respectively. Jabor Rabeah, Leibniz Institute for Catalysis, is gratefully acknowledged for EPR measurements. We are thankful to Nikolaos Moustakas, Leibniz Institute for Catalysis, for assistance in data processing.

Conflicts of Interest: The authors declare no conflict of interest.

References

1. Moustakas, N.G.; Strunk, J. Photocatalytic CO₂ Reduction on TiO₂-Based Materials under Controlled Reaction Conditions: Systematic Insights from a Literature Study. *Chem. Eur. J.* **2018**, *24*, 12739–12746. [CrossRef] [PubMed]
2. Kondratenko, E.V.; Mul, G.; Baltrusaitis, J.; Larrazábal, G.O.; Pérez-Ramírez, J. Status and perspectives of CO₂ conversion into fuels and chemicals by catalytic, photocatalytic and electrocatalytic processes. *Energy Environ. Sci.* **2013**, *6*, 3112–3135. [CrossRef]
3. Daghrir, R.; Drogui, P.; Robert, D. Modified TiO₂ for environmental photocatalytic applications: A review. *Ind. Eng. Chem. Res.* **2013**, *52*, 3581–3599. [CrossRef]
4. Xiong, Z.; Zhao, Y.; Zhang, J.; Zheng, C. Efficient photocatalytic reduction of CO₂ into liquid products over cerium doped titania nanoparticles synthesized by a sol-gel auto-ignited method. *Fuel Process. Technol.* **2015**, *135*, 6–13. [CrossRef]
5. Fattakhova-Rohlfing, D.; Zaleska, A.; Bein, T. Three-dimensional titanium dioxide nanomaterials. *Chem. Rev.* **2014**, *114*, 9487–9558. [CrossRef]
6. Cherevan, A.S.; Deilmann, L.; Weller, T.; Eder, D.; Marschall, R. Mesoporous Semiconductors: A New Model to Assess Accessible Surface Area and Increased Photocatalytic Activity? *ACS Appl. Energy Mater.* **2018**, *1*, 5787–5799. [CrossRef]

7. Zhang, R.; Elzatahry, A.A.; Al-Deyab, S.S.; Zhao, D. Mesoporous titania: From synthesis to application. *Nano Today* **2012**, *7*, 344–366. [[CrossRef](#)]
8. Zhang, W.; Tian, Y.; He, H.; Xu, L.; Li, W.; Zhao, D. Recent advances in the synthesis of hierarchically mesoporous TiO₂ materials for energy and environmental applications. *Natl. Sci. Rev.* **2020**, *7*, 1702–1725. [[CrossRef](#)]
9. Zhang, T.; Low, J.; Koh, K.; Yu, J.; Asefa, T. Mesoporous TiO₂ Comprising Small, Highly Crystalline Nanoparticles for Efficient CO₂ Reduction by H₂O. *ACS Sustain. Chem. Eng.* **2018**, *6*, 531–540. [[CrossRef](#)]
10. Lo, A.-Y.; Taghipour, F. Ordered mesoporous photocatalysts for CO₂ photoreduction. *J. Mater. Chem. A* **2021**, *9*, 26430–26453. [[CrossRef](#)]
11. Parlett, C.M.; Wilson, K.; Lee, A.F. Hierarchical porous materials: Catalytic applications. *Chem. Soc. Rev.* **2013**, *42*, 3876–3893. [[CrossRef](#)]
12. Ismail, A.A.; Bahnemann, D.W. Mesoporous titania photocatalysts: Preparation, characterization and reaction mechanisms. *J. Mater. Chem.* **2011**, *21*, 11686–11707. [[CrossRef](#)]
13. Bonelli, B.; Esposito, S.; Freyria, F.S. Mesoporous Titania: Synthesis, Properties and Comparison with Non-Porous Titania. In *Titanium Dioxide*; InTechOpen: Rijeka, Croatia, 2017.
14. Zimny, K.; Ghanbaja, J.; Carteret, C.; Stébé, M.-J.; Blin, J.-L. Highly ordered mesoporous titania with semi crystalline framework templated by large or small nonionic surfactants. *New J. Chem.* **2010**, *34*, 2113–2117. [[CrossRef](#)]
15. Zimny, K.; Roques-Carmes, T.; Carteret, C.; Stébé, M.; Blin, J. Synthesis and photoactivity of ordered mesoporous titania with a semicrystalline framework. *J. Phys. Chem. C* **2012**, *116*, 6585–6594. [[CrossRef](#)]
16. Mohammed, A.M.; Sebek, M.; Kreyenschulte, C.; Lund, H.; Rabeh, J.; Langer, P.; Strunk, J.; Steinfeldt, N. Effect of metal ion addition on structural characteristics and photocatalytic activity of ordered mesoporous titania. *J. Sol-Gel Sci. Technol.* **2019**, *91*, 539–551. [[CrossRef](#)]
17. Chen, L.; Li, Y.-J.; Peng, X.; Li, Z.-S.; Zeng, M.-X. Preparation and improved photocatalytic activity of ordered mesoporous TiO₂ by evaporation induced self-assembly technique using liquid crystal as template. *T. Nonferr. Metal. Soc.* **2014**, *24*, 1072–1078.
18. Zhang, W.; He, H.; Tian, Y.; Lan, K.; Liu, Q.; Wang, C.; Liu, Y.; Elzatahry, A.; Che, R.; Li, W.; et al. Synthesis of uniform ordered mesoporous TiO₂ microspheres with controllable phase junctions for efficient solar water splitting. *Chem. Sci.* **2019**, *10*, 1664–1670. [[CrossRef](#)]
19. Wang, T.; Meng, X.G.; Li, P.; Ouyang, S.X.; Chang, K.; Liu, G.G.; Mei, Z.W.; Ye, J.H. Photoreduction of CO₂ over the well-crystallized ordered mesoporous TiO₂ with the confined space effect. *Nano Energy* **2014**, *9*, 50–60. [[CrossRef](#)]
20. Lee, Y.Y.; Jung, H.S.; Kim, J.M.; Kang, Y.T. Photocatalytic CO₂ conversion on highly ordered mesoporous materials: Comparisons of metal oxides and compound semiconductors. *Appl. Catal. B-Environ.* **2018**, *224*, 594–601. [[CrossRef](#)]
21. Wang, T.; Meng, X.; Liu, G.; Chang, K.; Li, P.; Kang, Q.; Liu, L.; Li, M.; Ouyang, S.; Ye, J. In situ synthesis of ordered mesoporous Co-doped TiO₂ and its enhanced photocatalytic activity and selectivity for the reduction of CO₂. *J. Mater. Chem. A* **2015**, *3*, 9491–9501. [[CrossRef](#)]
22. Xue, H.; Wang, T.; Gong, H.; Guo, H.; Fan, X.; Gao, B.; Feng, Y.; Meng, X.; Huang, X.; He, J. Constructing Ordered Three-Dimensional TiO₂ Channels for Enhanced Visible-Light Photocatalytic Performance in CO₂ Conversion Induced by Au Nanoparticles. *Chem. Asian J.* **2018**, *13*, 577–583. [[CrossRef](#)] [[PubMed](#)]
23. Xiong, J.; Zhu, X.; Chen, Z.; Ren, Y.; Wang, W.; Han, C.; Li, W.; Li, S.; Cheng, G. Oxygen Vacancy and Metallic Silver Site Coinjection Associates Photocatalytic CO₂ Reduction upon Mesoporous NH₂-TiO₂ Nanoparticles Assembly. *Solar RRL* **2022**, *6*, 2200657. [[CrossRef](#)]
24. Sing, K.S.; Everett, D.H.; Haul, R.A.W.; Moscou, L.; Pierotti, R.A.; Rouquerol, J.; Siemieniewska, T. Reporting physisorption data for gas/solid systems with special reference to the determination of surface area and porosity (Recommendations 1984). *Pure Appl. Chem.* **1985**, *57*, 603–619. [[CrossRef](#)]
25. Zuas, O.; Budiman, H. Synthesis of nanostructured copper-doped titania and its properties. *Nano-Micro Lett.* **2013**, *5*, 26–33. [[CrossRef](#)]
26. Wang, Q.; Jin, R.; Zhang, M.; Gao, S. Solvothermal preparation of Fe-doped TiO₂ nanotube arrays for enhancement in visible light induced photoelectrochemical performance. *J. Alloys Compd.* **2017**, *690*, 139–144. [[CrossRef](#)]
27. Zhang, D. Chemical synthesis of Ni/TiO₂ nanophotocatalyst for UV/visible light assisted degradation of organic dye in aqueous solution. *J. Sol-Gel Sci. Technol.* **2011**, *58*, 312–318. [[CrossRef](#)]
28. Brik, M.; Srivastava, A.; Popov, A. A few common misconceptions in the interpretation of experimental spectroscopic data. *Opt. Mater.* **2022**, *127*, 112276. [[CrossRef](#)]
29. Jubu, P.; Yam, F.; Igba, V.; Beh, K. Tauc-plot scale and extrapolation effect on bandgap estimation from UV-vis-NIR data—a case study of β -Ga₂O₃. *J. Solid State Chem.* **2020**, *290*, 121576. [[CrossRef](#)]
30. Makuła, P.; Pacia, M.; Macyk, W. How to correctly determine the band gap energy of modified semiconductor photocatalysts based on UV-Vis spectra. *J. Phys. Chem. Lett.* **2018**, *9*, 6814–6817. [[CrossRef](#)]
31. Choudhury, B.; Dey, M.; Choudhury, A. Defect generation, d-d transition, and band gap reduction in Cu-doped TiO₂ nanoparticles. *Int. Nano Lett.* **2013**, *3*, 25. [[CrossRef](#)]
32. Park, S.-M.; Razzaq, A.; Park, Y.H.; Sorcar, S.; Park, Y.; Grimes, C.A.; In, S.-I. Hybrid Cu_xO-TiO₂ Heterostructured Composites for Photocatalytic CO₂ Reduction into Methane Using Solar Irradiation: Sunlight into Fuel. *ACS Omega* **2016**, *1*, 868–875. [[CrossRef](#)]

33. Anitha, B.; Khadar, M.A. Dopant concentration dependent magnetism of Cu-doped TiO₂ nanocrystals. *J. Nanopart. Res.* **2016**, *18*, 149. [[CrossRef](#)]
34. Colon, G.; Maicu, M.; Hidalgo, M.S.; Navio, J. Cu-doped TiO₂ systems with improved photocatalytic activity. *Appl. Catal. B* **2006**, *67*, 41–51. [[CrossRef](#)]
35. Li, G.; Dimitrijevic, N.M.; Chen, L.; Rajh, T.; Gray, K.A. Role of surface/interfacial Cu²⁺ sites in the photocatalytic activity of coupled CuO–TiO₂ nanocomposites. *J. Phys. Chem. C* **2008**, *112*, 19040–19044. [[CrossRef](#)]
36. Baltazar, P.; Lara, V.; Cordoba, G.; Arroyo, R. Kinetics of the amorphous—Anatase phase transformation in copper doped titanium oxide. *J. Sol-Gel Sci. Technol.* **2006**, *37*, 129–133. [[CrossRef](#)]
37. Yao, X.; Tang, C.; Ji, Z.; Dai, Y.; Cao, Y.; Gao, F.; Dong, L.; Chen, Y. Investigation of the physicochemical properties and catalytic activities of Ce 0.67 M 0.33 O₂ (M = Zr⁴⁺, Ti⁴⁺, Sr⁴⁺) solid solutions for NO removal by CO. *Catal. Sci. Technol.* **2013**, *3*, 688–698. [[CrossRef](#)]
38. Zeng, M.; Li, Y.; Mao, M.; Bai, J.; Ren, L.; Zhao, X. Synergetic effect between photocatalysis on TiO₂ and thermocatalysis on CeO₂ for gas-phase oxidation of benzene on TiO₂/CeO₂ nanocomposites. *ACS Catalysis* **2015**, *5*, 3278–3286. [[CrossRef](#)]
39. Deng, C.; Li, B.; Dong, L.; Zhang, F.; Fan, M.; Jin, G.; Gao, J.; Gao, L.; Zhang, F.; Zhou, X. NO reduction by CO over CuO supported on CeO₂-doped TiO₂: The effect of the amount of a few CeO₂. *Phys. Chem. Chem. Phys.* **2015**, *17*, 16092–16109. [[CrossRef](#)]
40. Dilla, M.; Schlägl, R.; Strunk, J. Photocatalytic CO₂ Reduction Under Continuous Flow High-Purity Conditions: Quantitative Evaluation of CH₄ Formation in the Steady-State. *ChemCatChem* **2017**, *9*, 696–704. [[CrossRef](#)]
41. Pougin, A.; Dilla, M.; Strunk, J. Identification and exclusion of intermediates of photocatalytic CO₂ reduction on TiO₂ under conditions of highest purity. *Phys. Chem. Chem. Phys.* **2016**, *18*, 10809–10817. [[CrossRef](#)]
42. Moustakas, N.G.; Lorenz, F.; Dilla, M.; Peppel, T.; Strunk, J. Pivotal Role of Holes in Photocatalytic CO₂ Reduction on TiO₂. *Chemistry* **2021**, *27*, 17213–17219. [[CrossRef](#)] [[PubMed](#)]

Disclaimer/Publisher’s Note: The statements, opinions and data contained in all publications are solely those of the individual author(s) and contributor(s) and not of MDPI and/or the editor(s). MDPI and/or the editor(s) disclaim responsibility for any injury to people or property resulting from any ideas, methods, instructions or products referred to in the content.